"STABILITY AND SEISMIC VULNERABILITY OF THE STYLITE TOWER AT UMM AR-RASAS „

Paolo Clemente[*,1], Giuseppe Delmonaco[2], Lucamaria Puzzilli[2], Fernando Saitta[1]

[1] ENEA Casaccia Research Centre, Via Anguillarese 301, 00123 Rome, Italy
[2] ISPRA – Dept. Geological Survey of Italy, Via Vitaliano Brancati 48, 00144 Rome, Italy

ABSTRACT

The stability and vulnerability analyses carried out on the Stylite tower at Umm ar–Rasas, Jordan, are presented in this paper. The tower is a unique example of this kind of structure still existing. The soil and the structural material were analyzed by means of in situ ex–perimental tests. These consisted of Schmidt–hammer tests on stone blocks and passive seismic measurements. The stability of the tower was first analyzed, assuming an elastic – perfect plastic behavior in compression for masonry. Then the push–over seismic analysis was carried out, which was based on a single–mode approach and a finite solid element modelling with a Drucker–Prager yield criterion for masonry. The work is propaedeutic to the design of a retrofit intervention.

1. INTRODUCTION

Masonry towers and columns were built in ancient cultures as religious structures, as in the case of minarets and bell towers of churches, or to celebrate military victories, as in the case of the Roman's columns. These structures are exposed to high risks even under low intensity earthquakes, because of the presence of no–tension material and their slenderness. The need of conservation of their historic and cultural value does not allow using ordinary strengthening techniques, used in common buildings. In fact, any in–tervention on a historic structure could determine the loss of its cultural value. On the other hand, the ab–sence of a suitable maintenance certainly determines its deterioration and finally its collapse. An accurate knowledge of a monumental structure and the site where it is located are needed to design a suitable restoration intervention and a maintenance plan for the future.

Several research studies are reported in the literature for masonry towers, both on experimental analysis and modelling.

Among the experimental studies, it is worth mentioning the contribution by Modena et al., [2002], which reports the field investigations on the damaged bell tower of the Cathedral of Monza, Italy, based on the characterization of materials and dynamic tests, and the repair and strengthening measures proposed. The same subject was addressed by Gentile and Saisi, [2007] with the definition and the updating of a finite element model on the basis of experimental data. Ivorra and Pallarés, [2006] report the dynamic characterization of the bell tower in a church in Valencia, Spain. Detailed studies, also based on experimental dynamic analysis by using ambient and traffic–induced vibrations, were carried out on the Coclid Columns in Rome [Bongiovanni et al., 2017a; Bongiovanni et al., 2014], which show the effect of past earthquakes, as well as on the Flaminio Obelisk [Bongiovanni et al., 1990], on the Lateran Obelisk [Buffarini et al., 2008; Buffarini et al., 2009], and on the Northern Wall of the Colosseum [Bongiovanni et al., 2017b]. Several experimental studies were also carried out on earthquake damage tower and constructions [Krstevska et al. 2010; Clemente et al. 2002]. A comprehensive presentation of the most interesting applications of Structural Health Monitoring in Italy was given by De Stefano et al., [2016].

Other relevant studies are related to modelling and structural analyses. Dogangun et al., [2008] carried out a linear dynamic analysis of three minarets of different height, modeled by means of solid finite elements. Oliveira et al., [2012] performed a linear dynamic analysis of several minarets in Istanbul with the support of experimental measurements. A stochastic analysis of the Ulu Mosque minaret under seismic and blast loadings was performed by Haciefendioğlu and Birinci, [2011]. Sarhosis et al., [2018] used and compared different approaches for the estimation of the seismic vulnerability of masonry towers.

Nonlinear analyses, involving models for materials and damage, have been carried out by different authors. A biaxial orthotropic hypo–elastic concrete model modified for masonry was used by Mortezaei et al., [2012] in the analysis of the mosque Masjed–e–Jame of Semnan (Iran), which contains a minaret. The work allowed demonstrating the nature of the present cracks, which was found to depend primarily on the ground settlement and showed the sensitivity of the building to ground settlement.

Peña et al., [2010] analyzed the Qutb Minar in New Delhi by means of both linear and nonlinear models,

and using solid, shell and beam finite element models and carried out nonlinear push–over and dynamic analyses using non–solid models, because of the large amount of the computational resources required. A smeared cracking model, with an exponential tension softening and constant shear retention was adopted, and a parabolic compressive behavior was assumed for masonry. Clemente et al., [2015] proposed the structural analysis of the leaning minaret at Jam, Afghanistan, considering both soil and masonry collapses, under different distributions of static loads along the height, proportionally increasing to the collapse values.

In this paper, the stability and the seismic vulnerability of the Stylite Tower at Umm ar–Rasas, which is a UNESCO World Heritage site in Jordan, are analyzed. It is the first known and architecturally intact example of this type of tower in this region of the Middle East, survived up to our age [DOA, 2002]. This makes the tower unique and its conservation of extreme importance. The structure presents damage related to the aging and to past earthquakes, which affected frequently the area [Sbeinati et al., 2005] In the framework of a comprehensive study of the structure, based on a preliminary evaluation of the material properties, the stability and seismic vulnerability analyses were carried out. The analysis focused mainly on the present structural health status and on the evaluation of the potential risk under the design earthquake scenario. This study represented a preliminary step toward a preservation effort leading to a proposal of a structural intervention. The proposal will also account for the experimental data obtained by other authors [Cozzolino et al., 2019]. The results here shown confirm the present precarious condition of the tower and the necessity of urgent and adequate interventions for its structural preservation.

2. THE STYLITE TOWER AND ITS SITE

The Byzantine Stylite Tower is sited about 1.2 km NW from the core of the archaeological site of Umm ar–Rasas (31.30'43.60"N; 35.55'18.92"E), approximately at 735 m a.s.l. (Figure 1). The tower was built in the first half of the 6th century A.D. and was originally surrounded by a wall. As well known, the stylites were Christian ascetic monks, who spent all their life in isolation, at the top of a tower, preaching, fasting and praying.

The tower is 13.5 m high. It has a square base cross–section with size b = 2.52 m, and presents externally 35 rows of trimmed local limestone blocks laid dry (Figure 2). Some of the external blocks are placed transversally and guarantee a connection with the internal fill.

FIGURE 1. Views of the Stylite Tower at Umm ar–Rasas.

The characteristics of the fill and its contribution to the structural capacity are not known. According to what can be seen from the lower chamber, the fill is made of blocks of similar material but not always squared. Any–way it is certainly effective in the lower part of the tower, where the presence of mortar among the stones guaran–tees collaboration with the external rows.

Considering the fill collaborating with the external blocks, the tower has a full cross–section except for a rec–tangular hole, eccentrically placed, for most of its height (section S3 in Figure 2, and Figure 3). This hole, about 30x40 cm size, was used by pilgrims to communicate with the monk. For the same reason, the tower presents also a small chamber at the basement, which reduces remarkably its effective cross–sections (section S2 in Figure 2, and Figure 4). Another very small hole was for the physiological needs of the monk, but its influence on the structural behavior is negligible.

Some of the stone blocks are cracked, especially those of the base layer. Furthermore, some blocks located at dif–ferent heights show relative displacements. The space be–tween them has been filled with stone slabs recently (Figure 5). The limestone blocks are also affected by dif–ferent nature and degree of weathering. The chamber originally placed at the top collapsed, along with the dome/vault, probably during a seismic event.

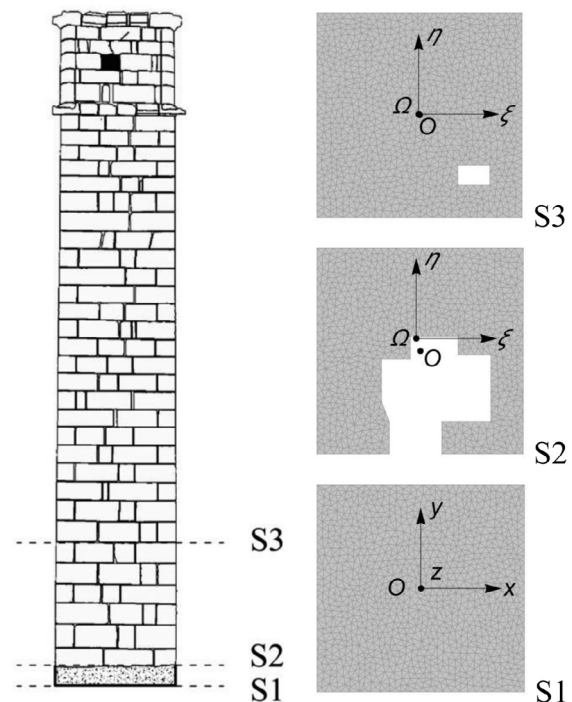The masonry tower is placed on a concrete slab, which

FIGURE 2. Three representative cross–sections of the tower.

has the same size of the tower base cross–section and whose extrados is at the same level of the ground sur–face. It is about 40 cm deep and is directly placed on the bedrock.

FIGURE 3. Rectangular hole, eccentrically placed.

FIGURE 4. Small chamber at the basement.

From a geological point of view, the area of Umm ar–Rasas is characterized by the presence of the Al–Hisa Phosporite formation (Campanian–Maastrichtian), 55–65 m thick and composed by three different members [Bender 1974; Tarawneh 1985; Powell 1989; Sadaqah et al., 2000]. The Bahiya coquina member is outcropping in the area. It is from few meters to 30 m thick and is mostly composed of fossiliferous limestone (rich in oyster shell, foraminifera, gasteropods and bivalves).

A first geotechnical campaign was performed in 2009, with boreholes and laboratory tests on rock materials (Uniaxial Compressive Strength, Point Load tests, rock specific gravity and absorption, chemical analysis) [Azzam and Doukh, 2009]. The blocks of the tower are of the same material, which will be described in detail in section 3.1.

The Stylite Tower at Umm ar–Rasas was heavily damaged by a strong earthquake occurred in 759 A.D., which caused the fall of the covering (dome and vaulted roof) and the upper part of the structure. The most recent destructive seismic event that affected the area was the Jericho earthquake, occurred on July 11th, 1927 (Ml = 6.2), which caused heavy damage in the close cities of Salt and Amman and probably also to the Stylite Tower [Avni, 1999; Zohar and Marco, 2012].

FIGURE 5. Space between the blocks has been filled with stone slabs.
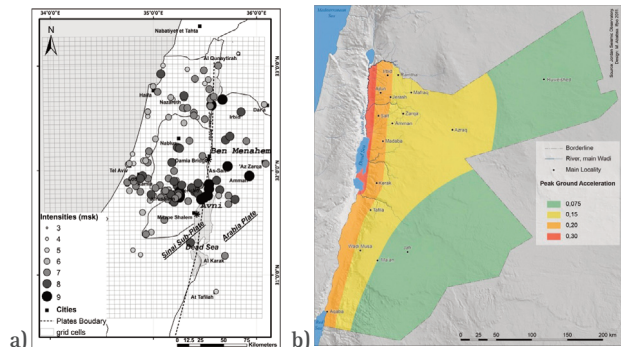

FIGURE 6. (a) Map of spatial distribution of intensities due to historical earthquakes (Avni, 1999); (b) Jordan seismic map (PGA in g).
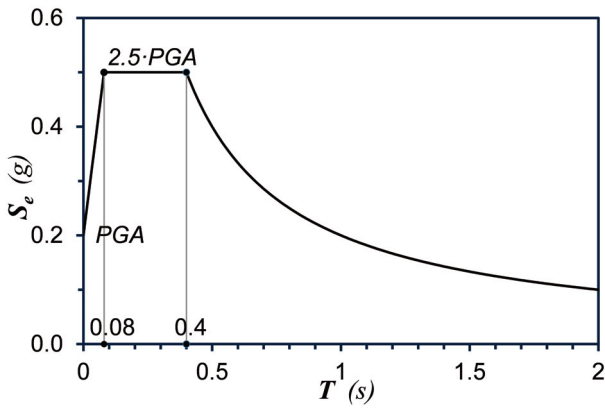
FIGURE 7. Elastic response spectrum at the site according to the Jordan code.

According to the Jordan seismic map (Figure 6) the area is characterized by high seismicity with a Peak Ground Acceleration of 0.2g and a shear waves velocity Vs = 760 ÷1500 m/s, typical of rigid soil [Menahem, 1991; Thomas et al., 2007]. The elastic response spectrum given by the Jordan technical code is shown in Figure 7, in which an amplification factor equal to 2.5 is con-sidered.

3. ON SITE EXPERIMENTAL ANALYSES

Between 2014 and 2015, some experimental analy-ses were carried out on the tower and on the ground. These consisted in Schmidt–hammer tests on stone blocks for in–situ assessment of the Uniaxial Compres-sive Strength (UCS) of the tower limestone material, and in four passive seismic measurements for a field eval-uation of the dynamic resonances of the ground. Being the Stylite Tower protected by the Jordanian Antiquity Law, destructive mechanical tests on the limestone blocks of the tower were not allowed.

3.1 UNIAXIAL COMPRESSIVE STRENGTH (UCS) AS-SESSMENT

The analysis of UCS was carried out on 31 stone blocks, which compose the first 3 external base rows of the tower, where major cracks are clearly visible. On each block, a non–destructive mechanical test using L–type Schmidt Rebound Hammer was performed [Miller, 1965, Deere and Miller 1966; Sachpazis, 1990; Katz et al., 2000].

The L–type Schmidt Rebound Hammer used in the field tests is characterized by a range of measurements 10÷250 N/mm^2 and an impact energy equal to 0.735 Nm. The reference international standards were ac-counted for the site test implementation and data analysis [ISRM 1981, ASTM D5873 2001, UNI EN
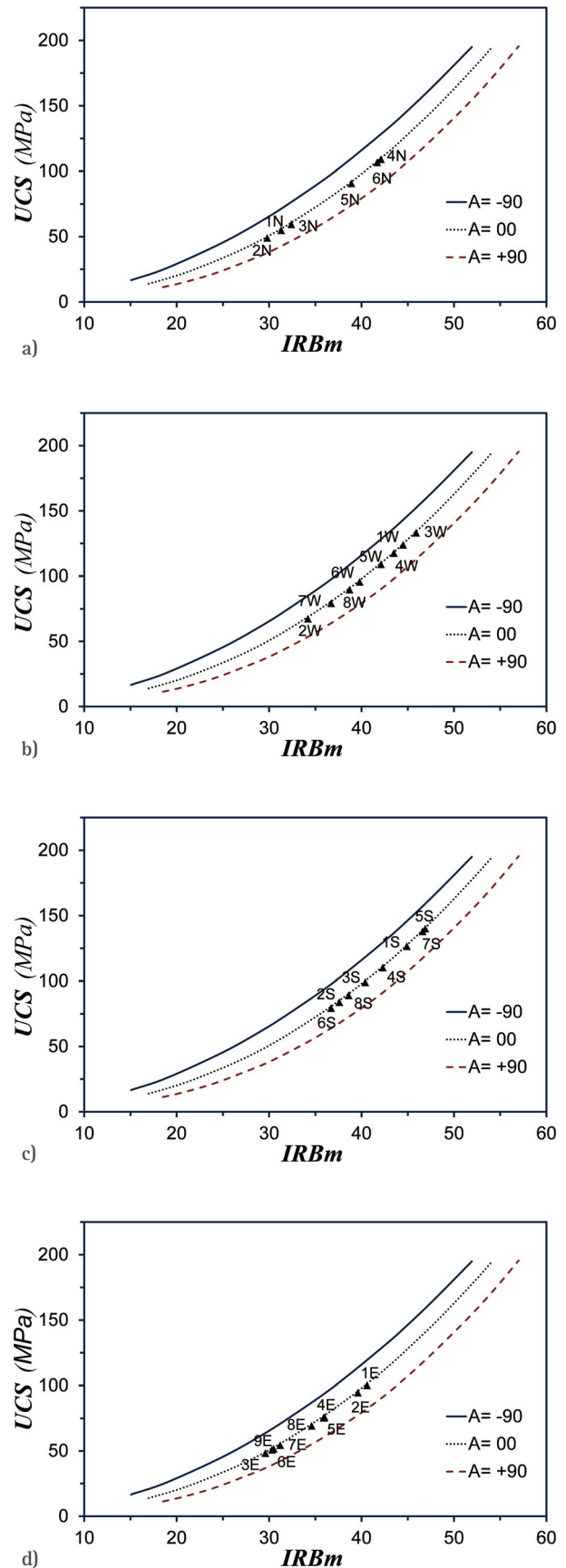

FIGURE 8. Correlation between Rebound Index (IRBm) – UCS (MPa) following direction of test execution vs. stone blocks for (a) North wall, (b) West wall, (c) South wall and (d) East wall.

Block No.	North wall UCS (N/mm²)	Cl.	Block No.	East Wall UCS (N/mm²)	Cl.	Block No.	South wall UCS (N/mm²)	Cl.	Block No.	West wall UCS (N/mm²)	Cl.
1N	54.8	R3	1E	100.1	R4	1S	126.4	R4	1W	123.8	R4
2N	48.9	R3	2E	94.5	R3	2S	83.8	R3	2W	67.3	R3
3N	59.4	R3	3E	48.2	R2	3S	99.0	R3	3W	133.1	R4
4N	108.9	R4	4E	75.8	R3	4S	110.1	R4	4W	117.5	R4
5N	90.7	R3	5E	75.3	R3	5S	139.9	R4	5W	108.9	R4
6N	106.5	R4	6E	50.8	R3	6S	79.3	R3	6W	95.6	R3
			7E	54.4	R3	7S	137.8	R4	7W	79.2	R3
			8E	69.1	R3	8S	89.1	R3	8W	89.6	R3
			9E	51.6	R3						

TABLE 1. UCS values calculated for single stone blocks and classifications according to the strength classes for rocks (ISRM, 1978). R1: very weak rock; R2: weak rock; R3: moderately weak rock; R4: strong rock; R5: very strong rock.
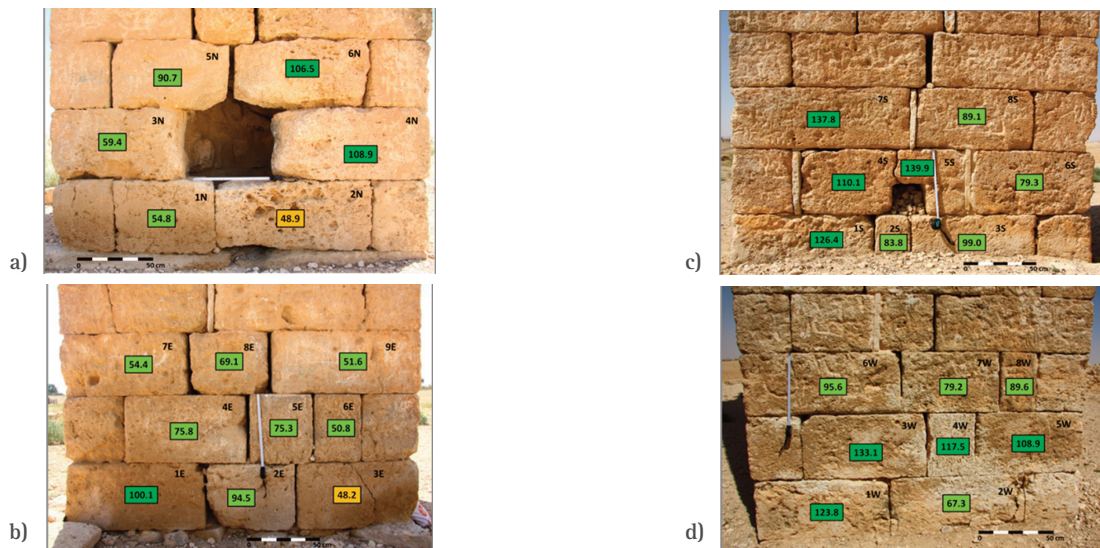

FIGURE 9. UCS values (N/mm2) of the limestone blocks represented as classes of strength (see Table 1) according to ISRM (1978) for (a) North wall, (b) East wall, (c) South wall and (d) West wall.

12504–2 2012]. The correlation between the uniaxial compressive strength UCS (N/mm²) and the rebound index IRBm is given by the calibration curves supplied by the hammer manufacturer, according to the relation UCS = a·IRBm^b, where a and b are calibration coefficients derived by destructive tests on rock samples.

For any stone block, a series of measurements were done, at points with a minimum relative distance of 50 mm. For each series, a set of 10 subsequent similar rebound values were selected for the assessment of UCS. The test points were chosen also on the basis of the external apparent quality of the material. Weathered and/or cracked portions of the stone blocks, when present, were considered in order to get the minimum value of UCS. The UCS value of each block was calculated as the mean of the UCS values corresponding to the ex-

perimental rebound values for the angle between the axis of the instrument and the horizontal direction (Figure 8). A total of 310 measurements of rebound values on 31 limestone blocks were analyzed (Table 1). The values obtained were classified according to the rock strength classes proposed by ISRM (1978), in order to provide a general view of the rock quality for any block analyzed. The same data are reported in Figure 9, where all single results are displayed according to the orientation of the walls (Figure 10).

As already mentioned, the quality of the rock depends strongly on lithological characteristics (i.e., texture, type and quality of cement, mineralogical content, presence and orientation of bedding, macro and micro–structural discontinuities) and on the presence and type of degradation (i.e., chemical, physical, mechanical weathering).
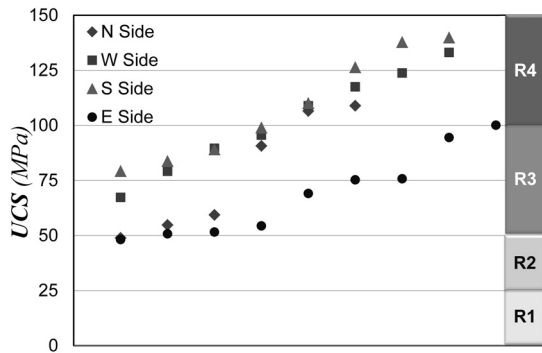
FIGURE 10. Diagram of UCS values and strength classes (ISRM, 1978) of the limestone blocks vs. wall orientation (R1= very weak rock; R2= weak rock; R3= moderately weak rock; R4= strong rock).

According to the results obtained, about 6% of samples are in R2 class, 58% and 34% are in R3 and R4 classes, respectively. This means that 29 out of 31 limestone blocks analyzed present a medium–high strength value. These results are coherent with UCS values obtained through laboratory analysis for intact limestone blocks of Al–Hisa Phosphorite formation [Naghoj et al., 2010]. As one can see, lower values of strength are related to the weathering conditions and to the cracks, which affect the blocks especially in the NE corner.

It is worth noting that the evaluation of the blocks strength is based only on the external toughness of them. The results are consistent with the usual strength value of this material. Anyway, a suitable reduction of the average value obtained experimentally will be considered in the numerical analysis.

3.2 PASSIVE SEISMIC MEASUREMENTS

Ambient noise recordings were carried out at four locations around the tower (Figure 11), using a Tromino (http://moho.world/) equipped with three orthogonal electrodynamic velocimeters. The Horizontal to Vertical

Spectral Ratio (HVSR) technique [Nakamura, 1989] was used in order to provide information on possible stratigraphic amplification and on the dynamic soil–structure interaction [Gallipoli et al., 2004; Gosar et al., 2010; Nakamura et al., 1999].

Tests lasting 20 minutes were carried out with a sampling rate of 128 points/s. Recording length and sampling rate were chosen on the basis of the expected frequency content in the HVSR spectra. Data were analyzed using the free and open source GEOPSY software (http://www.geopsy.org). The standardized procedure recommended in SESAME [2004] was implemented for both processing of the signals and validation of the retrieved HVSR curves. Furthermore, the analysis was performed in the frequency range 0.5⌉20 Hz, higher frequencies being not useful for practical engineering purposes.

An average H/V curve was retrieved for each location. Furthermore, the spectral ratios N/V and E/V between the single horizontal components (N for NS direction; E for WE direction) and the vertical component of the motion were also calculated for each location. Figure 12 reports the curves of E/V, N/V and H/V spectral ratios for all locations.

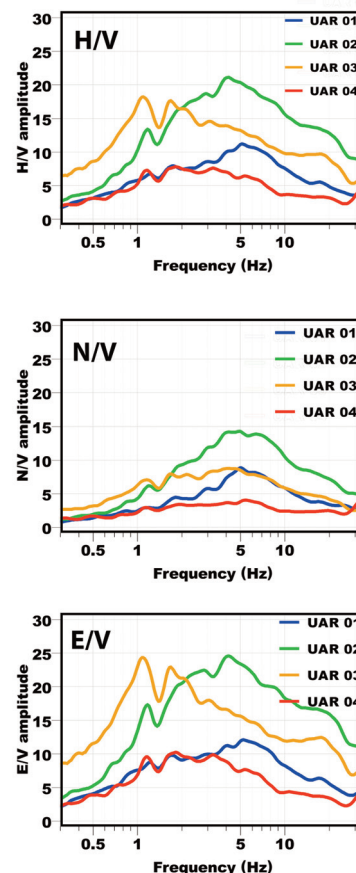FIGURE 11. Positions of passive seismic tests (UAR01–UAR04).

FIGURE 12. E/V, N/V and H/V amplitudes versus frequency for tests on the ground.

Very small amplitudes of all the signals were apparent in the spectra, especially for the vertical components. This has been mirrored in the high amplification values of the horizontal motions. Anyway this is out of the scope of this paper. The low energy associated to the spectra is also consistent with the characteristic of the site, which is low densely populated and far from usual anthropogenic sources of noise (such as traffic, industrial activities). On the other hand, this situation allowed to achieve more stable and reproducible HVSR curves (i.e., not affected by dominant artificial sources) that can be possibly referred to the fundamental resonance frequency of the site or to the frequency components induced by the tower [Margottini et al., 2015; Picotti et al., 2012].

Data elaboration highlighted two distinct ranges of frequency peaks. The first range, which is between 1.0 and 2.5 Hz, can be clearly seen in all the spectra, except for those of the N/V ratio at the positions UAR01 and UAR04. The second range is between 4.0 and 6.0 Hz.

Since all recording sites are very close to the tower, these frequency components are likely induced by the structure and are not related to the subsoil. Furthermore, the instrument was oriented to the geographic North during all the recordings. The HVSR for each horizontal direction was calculated and plotted in Figure 13 for all the locations. In Table 2 the resonance frequencies retrieved by processing the four recordings in terms of HVSR, NVSR and EVSR are reported. Differences at the four locations are apparent, especially considering the EVSR for the UAR03 and UAR04 sites.
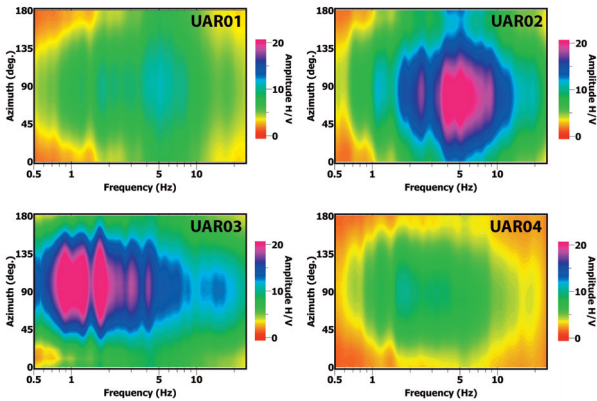

FIGURE 13. H/V diagrams for all directions for tests on the ground.

Location	HV (Hz)	NV (Hz)	EV (Hz)
UAR 1	5.2	5.3	5.1
UAR 2	5.0	4.9	5.1
UAR 3	1.7	4.2	1.8
UAR 4	2.0	5.7	2.0

TABLE 2. Resonance frequencies at the four locations.

4. PRESENT CONFIGURATION AND GLOBAL STABILITY

As already said, the masonry tower is supported by a concrete basement of the same size, which in turn is placed on the ground. Therefore, the global stability was first analysed by referring to the interface section S1 between the ground and the concrete slab. Then the section S2 at the base of the tower, i.e., the section between the masonry tower and the concrete basement, was analysed.

In order to have a understanding of the global stability, the tower was supposed to be infinitely rigid but the interface section, between the ground and the basement, was supposed to have an elastic – perfect plastic behavior with a compression strength f_t. On the basis of the experimental analysis on the local limestone before described, one can suppose that f_t is not lower than 10 N/mm^2 and the Young's modulus is not lower than 10000 N/mm^2 [Dweirj et al., 2017; Fener et al., 2005]. These values are also consistent with the characteristics of the concrete basement.

Assume the reference system 0xyz with the origin coincident with the centre of gravity of the square base cross–section S1, the two axes x and y parallel to the sides, and the axis z vertical. Including the basement and the covering, not present now, the structure would have a total weight W = 1800 kN and the center of gravity would be at the point with coordinates x_w = – 0.012 m, y_w = 0.018 m, z_w = 6.45 m. The internal forces at the interface section, between the concrete basement and the soil, are the following:

$$N = W = 1800kN \quad M_{wx} = -32.4kNm$$
$$M_{wy} = -21.6kNm \tag{1}$$

The eccentricity, given by the vector summation of the two eccentricities along x and y:

$$e_w = \sqrt{0.012^2 + 0.018^2} = 0.021m \tag{2}$$

is internal to the core of the squared cross–section. In the hypothesis of elastic behavior, the cross–section S1 is fully compressed and, therefore, totally effective. The corresponding maximum and minimum stresses are σ_{max} = 0.29 N/mm^2 and σ_{min} = 0.26 N/mm^2, respectively. Being $\sigma_{max} < f_t$, the hypothesis of linear elastic behavior for S1 in the present configuration is correct.

Assuming the model of rigid foundation on elastic half space with Young's modulus E and Poisson's ratio

ν, the rotational and vertical stiffness, respectively, are given by [Desideri et al., 1997]:

$$k_{\alpha 0} = \frac{E}{\left(1-\nu^2\right)} \cdot \frac{b^3}{I_\alpha} \qquad k_w = \frac{E}{\left(1-\nu^2\right)} \cdot \frac{b}{I_w} \qquad (3)$$

For a squared cross–section, b is the size, I_α = 3.8 and I_w = 0.87. Due to the very high value of the elastic modulus of the soil, the safety degree against instability is very high, apparently ensuring the global stability of the tower.

Actually, this result could give a false idea about the safety of the tower. Therefore, to complete the check of the global stability, it is useful to refer to the interface section S2 between the masonry tower and the concrete basement, for two basic reasons:

1) there are no connections between the tower and its basement;
2) S2 is the most vulnerable masonry cross–section, due to its reduced effective area.

The nonlinear behaviour of S2 is first analysed, then the model of rigid tower supported by an elastic–plastic cushion is considered as reported in the following section. This cushion simulates the interaction between the masonry base section and the rigid concrete slab.

4.1 LIMIT BEHAVIOUR OF THE BASE CROSS-SECTION S2

Assume the reference system $\Omega\xi\eta$ with the origin coincident with the centre of gravity of the effective cross–section at S2, and the two axes ξ and η are parallel to x and y, respectively (Figure 2). The coordinates of Ω in the Oxy system are x_Ω = –0.047 m and y_Ω = 0.154 m, respectively.

The masonry is supposed to have an elastic – perfect plastic behavior in compression with a strength f_m, but no tension resistance. Therefore, the nonlinear constitutive equations are the following (E_m = Young's modulus of masonry):

$$\sigma(\xi,\eta) = \begin{cases} 0 & \varepsilon < 0 \\ E_m \varepsilon(\xi,\eta) & 0 \le \varepsilon \le f_m / E_m \\ f_m & \varepsilon > f_m / E_m \end{cases} \qquad (4)$$

Three limit states must be considered, relative to the following stress conditions:

1) compression stress equal to zero at one edge (limit state LS1);
2) compression stress equal to f_m at one edge (limit state LS2);
3) effective cross–section uniformly compressed with stress equal to f_m (limit state LS3).

The cross–section being quite irregular, a general method was used to construct the corresponding limit domains. Assuming the hypothesis of planar cross–section in the deformed state, for any given position of the axial force N, and so for given values of the internal forces N, M_ξ and M_η, the strain in any point of the cross–section is given by:

$$\varepsilon(\xi,\eta) = \varepsilon_\Omega - c_\xi \eta + c_\eta \xi \qquad (5)$$

where ε_Ω is the strain at the centre of gravity Ω, and c_ξ and c_η are two parameters that define the cross–section plane and assume the meaning of curvatures with reference to ξ and η axes, respectively. The corresponding stresses must respect the equilibrium conditions:

$$N = \int\sigma(\xi,\eta)dA \quad M_\xi = -\int_A \sigma(\xi,\eta) \cdot \eta\, dA$$
$$M_\eta = \int_A \sigma(\xi,\eta) \cdot \xi\, dA \qquad (6)$$

where the integrals are extended to the cross–section A. Eqs. (6) represent, after substitution, a system of nonlinear equations in the unknowns ε_Ω, c_ξ and c_η, which allow finding out the cross section plane and the neutral axis position.

The limit domains were obtained as follows. For any fixed value of the axial force N and for each direction in the cross–section plane, the eccentricity was increased from zero to the collapse value and the corresponding neutral axis position and the stress distribution were obtained. It is worth noting that the direction of the neutral axis is not necessarily constant when eccentricity increases along one straight line. The eccentricities corresponding to the three limit states LS1, LS2 and LS3 were individualized.

To obtain the complete limit surfaces, several values of N and eccentricity directions varying from 0 to 2π were considered. Figure 14 shows the three non–dimensional limit surfaces LS1, LS2 and LS3. These refer to the non–dimensional parameters $\hat{N} = N/N_0$, $\hat{M}_\xi = M_\xi/M_0$ and $\hat{M}_\eta = M_\eta/M_0$, where N_0 and M_0 are the axial force and the maximum bending moment corresponding to a fully yielded squared cross–section, respectively:

$$N_0 = b^2 f_m \qquad M_0 = b^3 f_m/8 \qquad (7)$$

For the purposes of this study, significant representations of the limit surfaces are their intersections with:

1) the plane $\hat{M}_\eta / \hat{M}_\xi$ = 0.26 (Figure 15), corresponding to the variation of the eccentricity along the straight line r, passing through the origin Ω and the present stress point P (see Figure 17);

2) the plane $\hat{N} = W/N_0$, parallel to plane $OM_\xi \hat{M}_\eta$; in Figure 16 the points that could represent the pres–ent configuration are shown, each of them is rel–ative to a values of f_m.
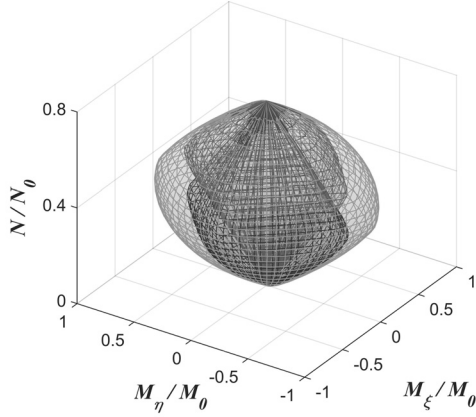

FIGURE 14. Limit surfaces LS1, LS2 and LS3 of the cross–sec–tion S2.
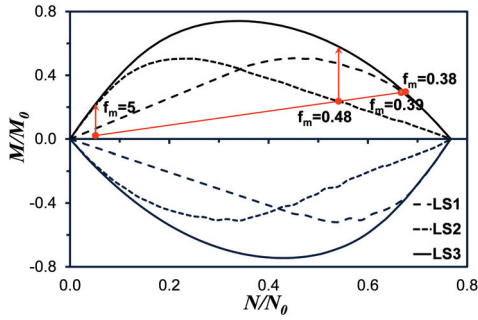

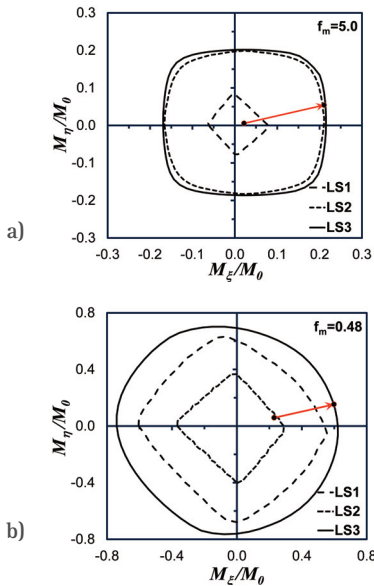FIGURE 15. Intersections of the limit surfaces with the plane $M_\eta/M_\xi = 0.26$.

FIGURE 16. Intersections of the limit surfaces with (a) the plane $\hat{N} = W/N_0 = 0.051$ and (b) the plane $\hat{N} = W/N_0 = 0.541$ parallel to O M_ξ/M_η and corresponding load paths.
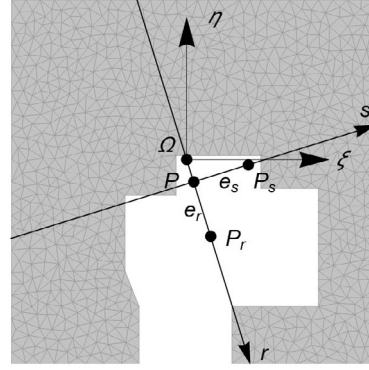
FIGURE 17. S2 cross–section and reference systems.

5. NONLINEAR ANALYSIS AND STABILITY AS-SESSMENT

The experimental analysis described above demon–strated that the limestone blocks present very dispersed strength values, with the lower values concentrated in the North and East walls. This occurrence suggested to assume a compression strength of the stone very close to the lower experimental value.

Consequently, for the Jordanian building limestone masonry of the tower one can reasonably assume a strength in the range $5 \div 10$ N/mm^2, and a correspon–ding Young's modulus between 5000 and 10000 N/mm^2 [Naghoj et al., 2010]. These ranges account for the ab–sence of the mortar or its bad quality, the irregularity of the joints and the absence of transversal connections or their non–effectiveness. Both the lower and upper limit values were considered in this study.

Consider the already mentioned oriented straight line r (passing through Ω and P, characterized by $\hat{M}_\eta / \hat{M}_\xi = 0.26$) and the oriented straight line s, passing through Ω and orthogonal to it (Figure 17). The curva–tures c_r and c_s, and the internal bending moments M_r and M_s, respectively, were referred to them.

If $\hat{N}$ is fixed and the eccentricity e_r varies along r from its present value at P, the loading path is repre–sented, in the plane $\hat{M}_\eta / \hat{M}_\xi = 0.26$, by a straight line starting from the point corresponding to the actual stress condition and orthogonal to $\hat{N}$ axis. For $f_m = 5.0$ N/mm^2, it is $\hat{N} = W/N_0 = 0.051$ and the corresponding loading path is shown in Figure 15.

In Figure 16a, the same stress path is the straight line $\hat{M}_\eta / \hat{M}_\xi = 0.26$. As one can see (Figure 15), LS1 occurs before LS2 in the lower range of $\hat{N}$ values. On the con–trary, LS2 occurs first in the higher range of $\hat{N}$. The value of $\hat{N}$ that separates the two behaviors is different for M positive or negative, because of the non–sym–metry of the cross–section S2.

Figure 18a shows the values of the curvatures c_s and c_r versus the non–dimensional eccentricity e_r/b, for $f_m = 5.0$ N/mm^2 (with $E = 5000$ N/mm^2) and $f_m = 10.0$ N/mm^2 (with $E = 10000$ N/mm^2). As one can see c_s in–creases significantly with e_r, while c_r keeps low values. Also the case of eccentricity $e_{s'}$, varying along the straight line s', parallel to s and passing through Ω, was consid–ered (Figure 17). In this case c_r increases significantly, while c_s assumes low values (Figure 18b).

a)

b)
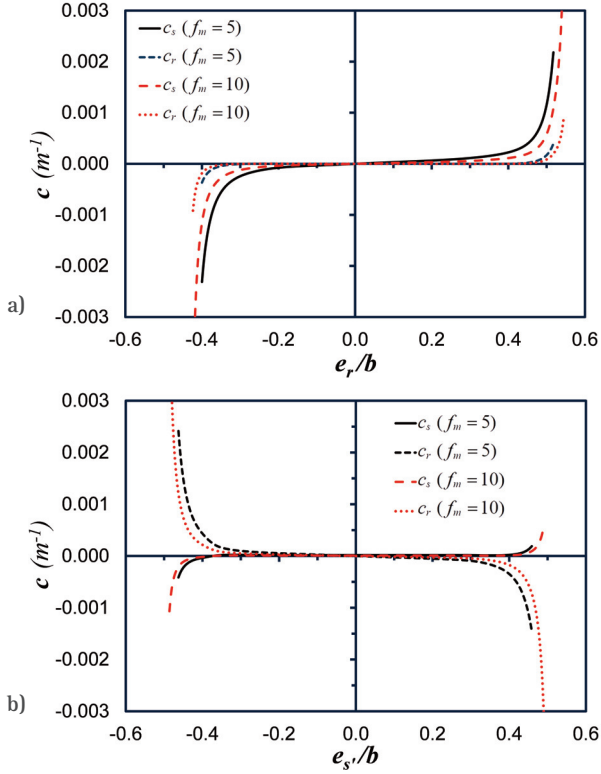
FIGURE 18. Curvature components versus eccentricity along: (a) initial direction ($M_\eta /M_\xi = 0.26$) and (b) orthog–onal ($M_\xi / M_\eta = 0.26$).

From the curvatures c_s and c_r, the rotation angles α_s and α_r were derived, assuming the plastic zone extended from S2 to S3, where the effective cross–section can be supposed to be the same of S2. The bending moment $\hat{M}_s$ is plotted in Figure 19a versus the bending rotation α_s, for the two considered values of f_m (and the corresponding values of E). Figure 19b shows the corresponding bend–ing moment $\hat{M}_r$ versus the bending rotation α_r, for the two considered values of f_m (and the corresponding val–ues of E). In Figures 20–22 the strain and stress diagrams for the case with eccentricity increasing along the straight line r and corresponding to the three limit states LS1, LS2 and LS3, respectively, are plotted.

If the increment of the bending moment M is related to a horizontal seismic acceleration a(z), the resultant force, applied at z_F from the base section (Figure 23), is:

$$F = \int_0^H m(z) \cdot a(z) \cdot dz \qquad (8)$$

From the equilibrium condition one can deduce the relation between F/W and the rotation α at the base (where the eccentricity e is a function of the rotation α):

$$\frac{F}{W} = \frac{1}{z_F} (e - z_w \cdot \alpha) \qquad (9)$$

The generalized displacement d is deduced as ratio between the work L of the external load and the force F:

$$d = \frac{L}{F} = \frac{\int_0^H m(z) \cdot a(z) \cdot d(z) \cdot dz}{\int_0^H m(z) \cdot a(z) \cdot dz} \qquad (10)$$

In Figures 24, the characteristic curves F/W versus the generalized displacement d, are plotted for the two values of f_m (and the corresponding E), for the case of eccentricity increasing along the direction r and along the direction s , respectively. As one can see, the max–imum value of F/W, which represents the horizontal ac–celeration, is very low if compared with the acceleration spectral amplitudes at the site, shown in Figure 7.
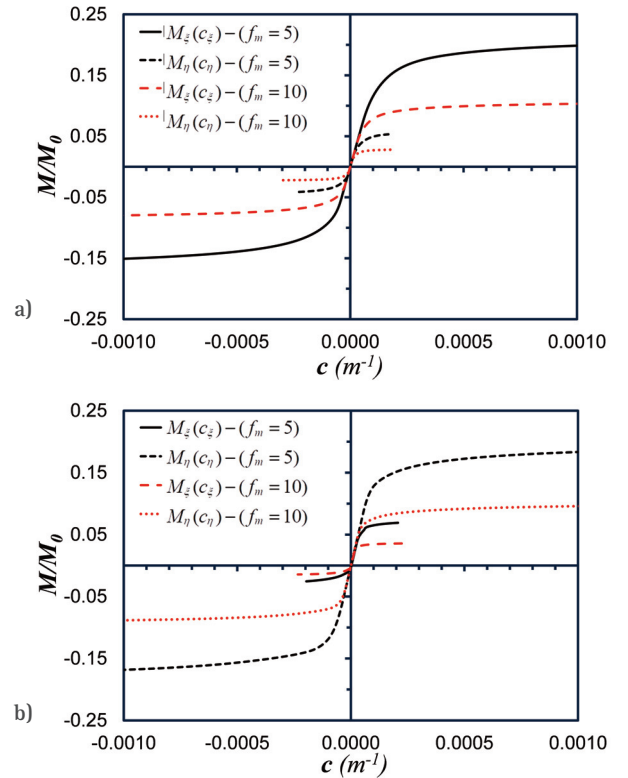

a)

b)

FIGURE 19. M/M_0 versus α for (a) initial direction ($M_\eta /M_\xi = 0.26$) and (b) orthogonal ($M_\xi / M_\eta = 0.26$), assuming as length of the plastic zone the height of the camber at the bottom.
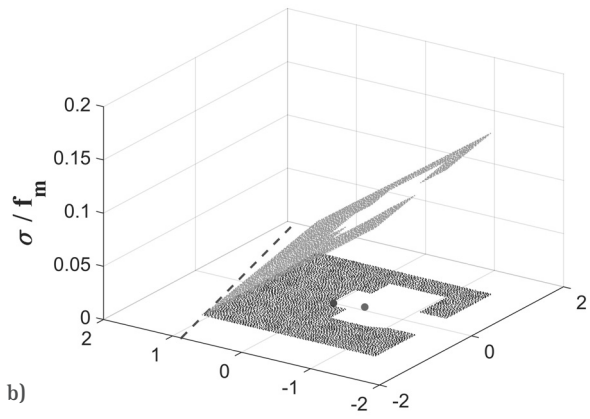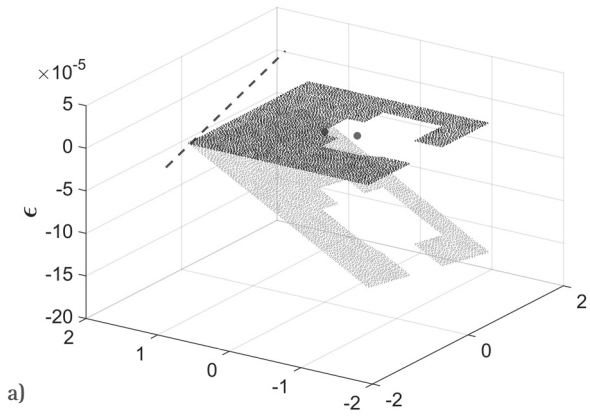
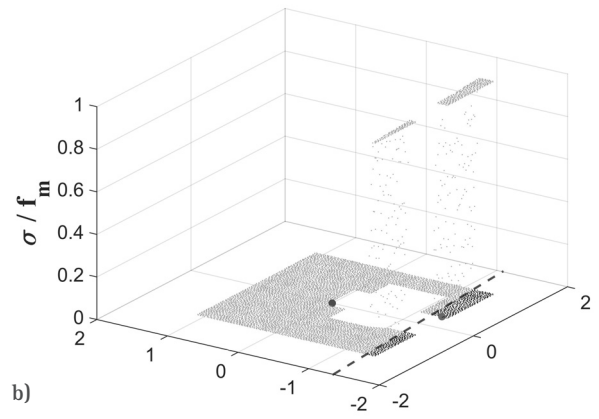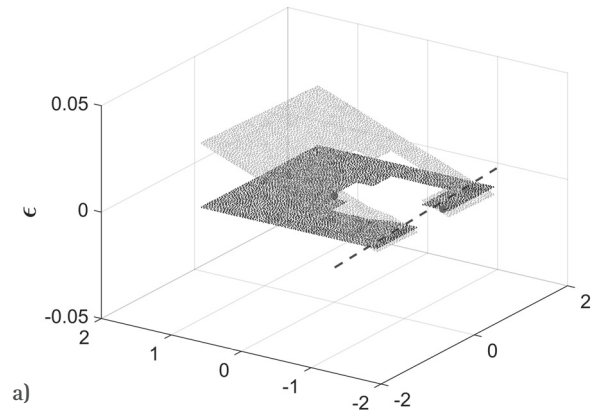**FIGURE 20.** (a) Strain and (b) stress distributions at LS1 (e=0.4 m).

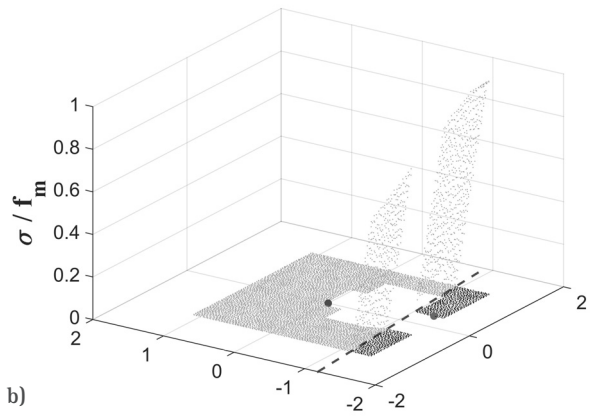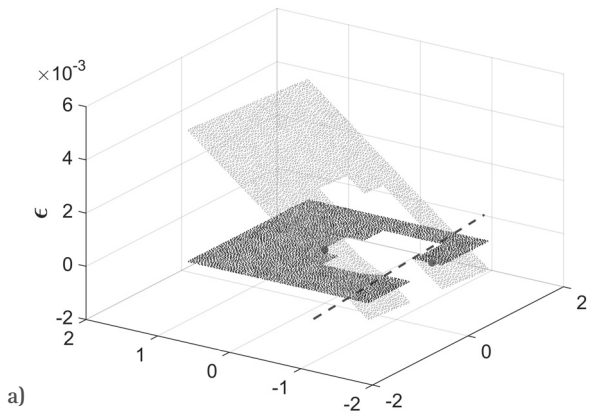**FIGURE 22.** (a) Strain and (b) stress distributions at LS1 (e=1.36 m).

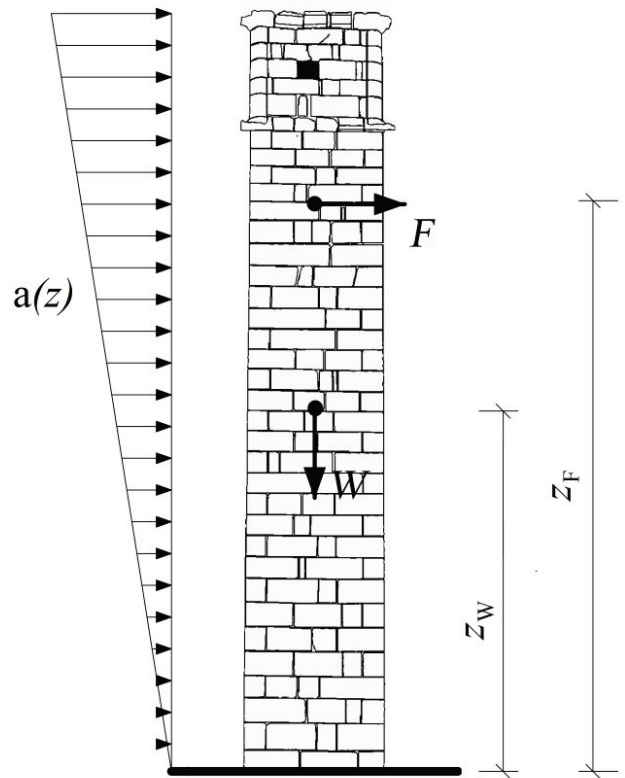**FIGURE 21.** (a) Strain and (b) stress distributions at LS2 (e=1.32 m).

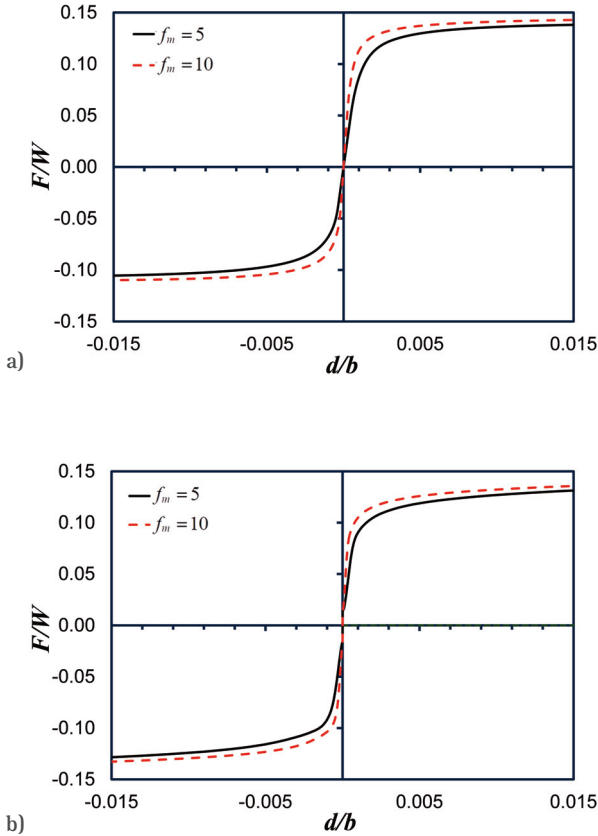**FIGURE 23.** Load condition in the rigid model.

FIGURE 22. *F/W* versus normalized displacement *d/b* for the cases of eccentricity increasing (a) along the direction *r* and (b) along the direction *s'*.

5.1 INFLUENCE OF THE COMPRESSION STRENGTH OF MASONRY

The hypothesis of $f_m = 5.0 \ N/mm^2$ is certainly on the safe side, but it is interesting to analyze how the previous evaluations are modified assuming lower values of f_m.

The limit domains have been represented in a non–dimensional form. This choice allows a fast representation of the safety conditions for different values of the masonry strength. The stress points corresponding to different values of f_m are all on a straight line, characterized by the ratio between the total bending moment and the axial force (Figure 15). The values of f_m that correspond to the intersections of this straight line with the limit domains are of particular interest:

1) if $f_m = 0.48 \ N/mm^2$, then the base section is at LS2 in the present situation (see also Figure16b),
2) if $f_m = 0.39 \ N/mm^2$, the section would be at LS1,
3) if $f_m = 0.38 \ N/mm^2$, the section would be at LS3.

All these values are much lower than the lower limit of the range of the compressive strength; therefore, in the present state, the base section can be considered safe.

6. NUMERICAL MODAL AND PUSH OVER ANALYSIS

A finite element model was set up with Ansys® computer code, using SOLID65 elements. The size of the elements was set sufficiently small to have not significant variation of the considered frequencies for further reduction of the element size.

The tower was supposed to be fixed at its base. The modal analysis gave the first 6 frequencies, reported in Table 3. For the successive nonlinear analysis it is important to note that the first modal shape presents prevalent displacement along *y* axis, while the second modal shape has prevalent displacements along *x* axis. The third mode is torsional and the higher modes are similar to the higher modes of a cantilever.

Mode	f (Hz)	Prevalent motion
1	3.42	y
2	3.54	x
3	16.13	torsional
4	17.71	y
5	17.98	x
6	27.91	z
7	40.84	xy

TABLE 3. Numerical frequencies.

As previously mentioned, the blocks along the perimeter of the tower are laid dry, whereas the internal rubble stones, at least in the lower part of the tower, are laid by mortar and holds some cohesion. The limestone is characterized by an internal friction coefficient higher than 0.69 [Al–Shayea, 2004] and the friction coefficient obtained experimentally in the case of sliding surfaces of limestone rocks is about 0.85 [Byerlee, 1978]. However, the behavior of the masonry is somewhat different, depending on the arrangement of the blocks, the roughness of the surfaces and the composition of units and joints. The influence of the arrangement of units, i.e. the micro–scale, on the response of masonry walls is discussed in Vasconcelos and Lourenço [2009], where the variation of the friction coefficient is shown for dry, irregular and rubble masonry. The response under horizontal forces for the case of dry masonry can be represented by a quasi bilinear behaviour.

On the basis of the accuracy desired in the numeri–cal models, different scales of representation can be considered [Angelillo et al., 2014].

A continuum model, based on smearing of units and joints, was chosen for the nonlinear analysis of the tower. The masonry was supposed to have an elastic – perfect plastic behavior, with a Drucker–Prager limit domain for 3–D stress states. A reasonable value of the cohesion, $c = 0.1$ N/mm^2, was assumed. For the friction coefficient, two values were considered, $\mu = 0.6$ and $\mu = 0.75$, respectively. Finally, a zero value for the di–latancy was assumed.

It is well known that the push–over analysis con–sists in submitting the structure to an incremental dis–tribution of forces. These are obtained as the product between the masses and an acceleration distribution at each joint. The acceleration distribution simulates one or more modal shapes of the structure itself. The results are described in terms of a force–displacement curve of the equivalent elastic–plastic single degree of freedom system [Fajfar 2000, Chopra & Goel 2002].

In this case two pushover analyses were carried out, by applying an incremental distribution of forces sim–ulating the first and the second modal shape, respec–tively, which are shown in Figure 25. The force $F_n^* = V_{bn}/\Gamma_n$ was obtained by dividing the base shear V_{bn} by the participation factor Γ_n of the n-th mode. The dis–placement D_n^* coincides with the already mentioned generalized displacement d under the assumed load dis–tribution. The curve was then bi–linearized by means of an energy equivalence.
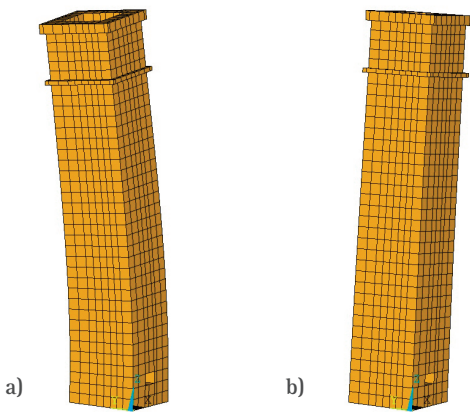

FIGURE 25. (a) First mode, (b) second mode.

The period of the equivalent oscillator is given by (y indicates quantities at yielding):

$$T_n^* = 2\pi \sqrt{\frac{L_n D_{ny}^*}{F_{ny}^*}} \qquad (11)$$

where $L_n = \Gamma_n M_n$ and M_n is the modal mass. The ca–pacity curve is obtained dividing the force F^* of the F^*-D^* curve by M_n. The reduction factor R_μ of the elastic spectrum is obtained as the ratio between the spectral acceleration of the elastic spectrum and the acceleration at post–yielding.

If the elastic period $T_n^* \geq T_C$ (in the elastic response spectrum, T_C separates the range with constant accel–eration from the range with constant velocity), then the inelastic displacement demand $S_d(T_n^*)$ coincides with the elastic one S_{de}, otherwise [Fajfar 2000]:

$$S_d = \frac{S_{de}}{R_\mu}\left[1 + (R_\mu - 1)\frac{T_c}{T_n}\right] \qquad (12)$$

In Figures 26 the force–displacement curves for $c = 0.1$ N/mm^2 and $\mu = 0.6$ are plotted, for force distribu–tions simulating mode 1 and mode 2, respectively. Anal–ogously, Figures 27 show the force–displacement curves for $c = 0.1$ N/mm^2 and $\mu = 0.75$, for the same force distri–butions. The non–symmetric resistance for forces simu–lating mode 1 (prevalent forces along y direction) is apparent, due to the absence of symmetry in the section at the base of the tower. The difference for mode 2 (prevalent forces along x direction) is less evident.
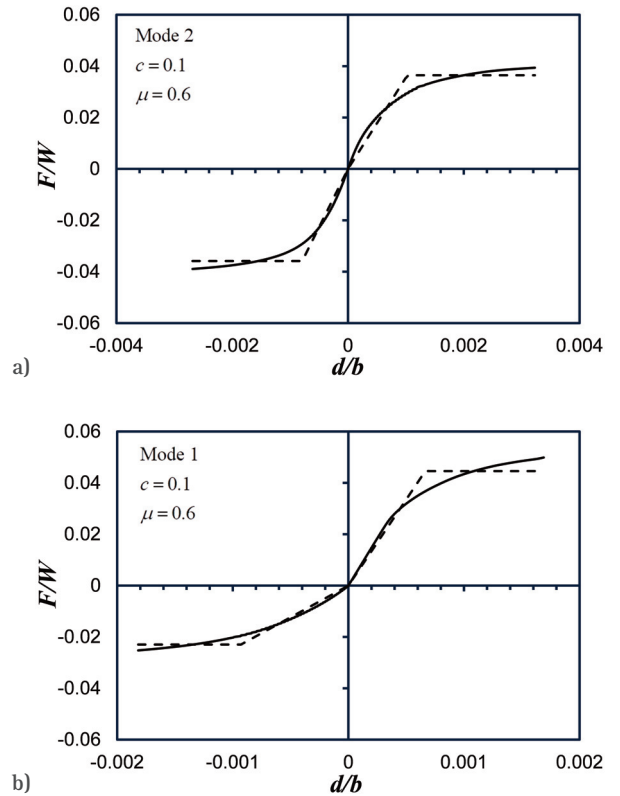

FIGURE 26. Base shear versus normalized displacement, for $c = 0.1$ N/mm^2 and $\mu = \mathrm{tg}\varphi = 0.6$ for (a) x direction or (b) y di–rection.

a)

b)

FIGURE 27. Base shear versus normalized displacement, for $c = 0.1$ N/mm^2 and $\mu = \text{tg}\varphi = 0.75$ for (a) x direction or (b) y di–rection.
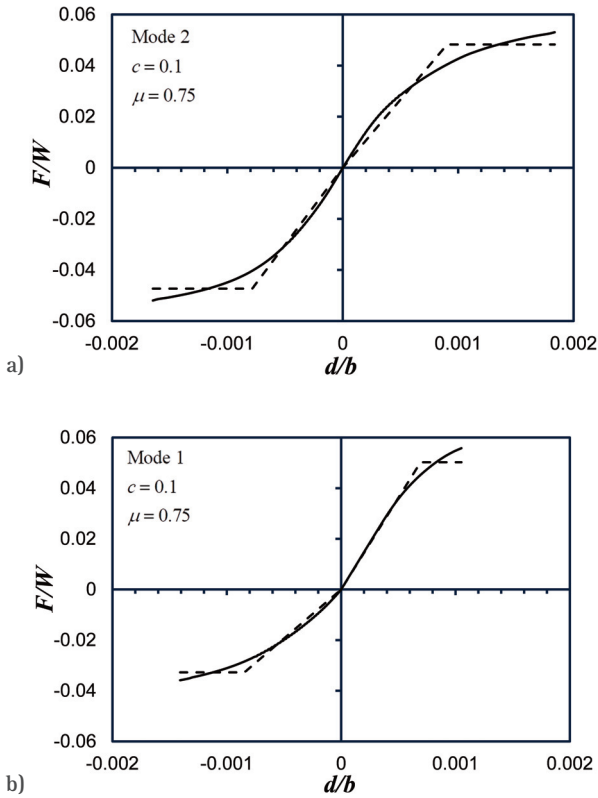
The plastic strain intensity at collapse are shown in Figures 28, for forces simulating the first and the sec–ond mode, respectively. The plastic strain is concen–trated at the walls of the base chamber, whereas the upper part of the tower remains in the elastic range. This result is consistent with the hypotheses assumed in the simplified model of the tower used for the stabil–ity analysis.

In all the cases the seismic capacity is very low if compared to the seismic demand given by the code (Figure 7). Figure 28 reports the S_a-S_d elastic and in–elastic spectra, with the capacity bi–linear curve, for the case $c = 0.1$ N/mm^2 and $\mu = 0.75$, and forces proportional to the first modal shape.

To investigate the influence of the two parameters c and μ on the capacity, the analysis was carried out also with different values of them. In general, higher values of the displacement capacity were related to higher values of the cohesion and lower values of μ. In Figure 29 the capacity curve, obtained with $c = 0.3$ N/mm^2 and $\mu = 0.36$, is compared with the elastic and inelastic spectra of the Jordan code at the site. In the same figure also the elastic and inelastic spectra for which the capacity is exactly equal to the demand are reported. They were obtained for a peak ground accel–eration of only 0.137g.
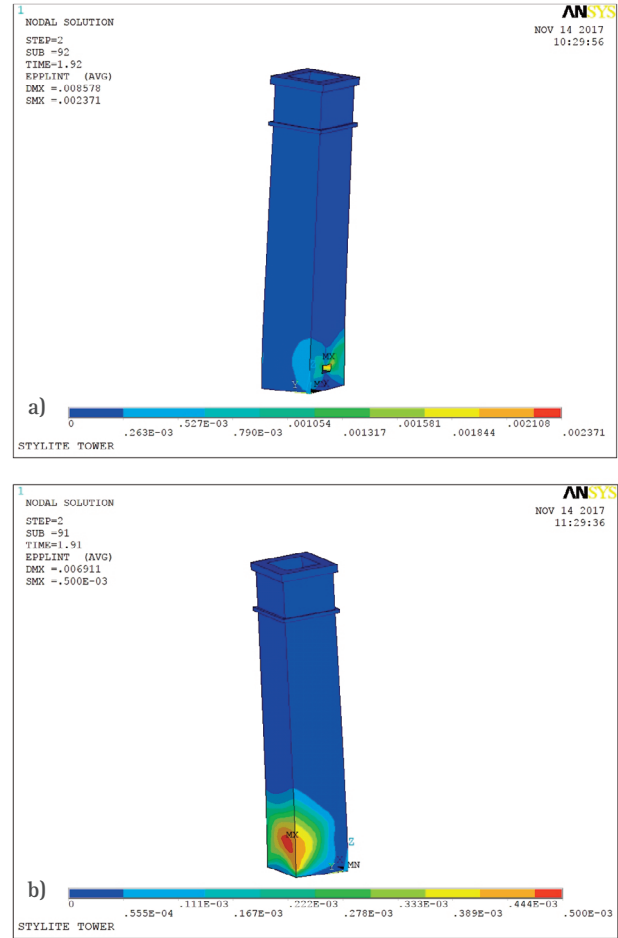

FIGURE 28. Plastic strain intensity at collapse for prevalent forces in y–direction (first mode) with (a) positive sign and (b) negative sign.
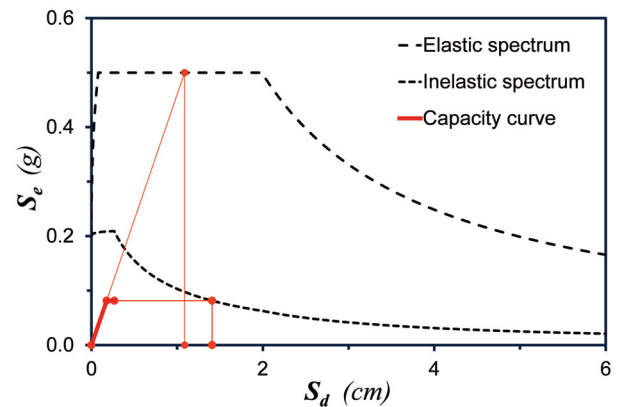

FIGURE 29. S_a-S_d elastic (continuous) and inelastic (dashed) spec–tra, with the capacity bi–linear curve (gray) for the case c = 0.1 N/mm_2 and forces proportional to $\mathbf{m}\phi_2$ (prevalent x direction).

7. CONCLUSIONS

The stability and the seismic vulnerability analyses

carried out on the Stylite tower at Umm ar–Rasas, Jordan, have been presented in this paper. The local lithology and the mechanical characteristics of the material were assessed by means of in situ experimental tests. Reasonable strength and deformability characteristics of the masonry were derived reducing conveniently those of the stone units, according to the available literature.

Two models were considered for the structural analysis. In the first one the tower was assumed infinitely rigid, but supported by an elastic – plastic cushion at its base. This model is justified by the presence of a chamber at the tower base, which reduces significantly the effective cross–section area for the portion of the tower between sections S2 and S3. The domains related to the limit states for this section of the tower were numerically derived in terms of internal forces, evaluating the safety in the present stress state and under eccentricity of the dead load varying along selected straight lines in the cross–section. Assuming that the eccentricity was due to a triangular horizontal acceleration diagram, acting along the rigid tower, the characteristic curves (i.e., generalized force – generalized displacement) were plotted with reference to two values of strength of the masonry. The comparison with the seismic actions, given by the Jordan code for the site, shows a capacity in terms of forces of about 25% of the demand.

The second model was a finite element model, in which solid elements were used. The material was characterized by an elastic–plastic behavior and a Drucker–Prager limit domain for three–dimensional stress states. 3–D load conditions were considered, using accelerations proportional to the first two modal shapes. Force–displacement capacity curves were obtained by incremental nonlinear static analysis using reasonable values of the cohesion and the friction. The curves show a very low capacity of the tower under seismic actions. Better results were obtained with higher values of the cohesion and with lower values of the friction coefficient, which correspond to more ductile behavior.

On the basis of the above results, possible proposals for the retrofit of the tower should include the improvement of the masonry characteristics, i.e., the increasing of cohesion, and of the bending resistance of the tower, which could be obtained resorting to pretension in order to increase the axial force.

REFERENCES

Al–Shayea N.A. (2004). Effects of testing methods and conditions on the elastic properties of limestone rock. Engineering Geology, 74, 139–156.

Angelillo M., P.B. Lourenço and G. Milani (2014). Masonry behaviour and modelling. In Angelillo M (ed) Mechanics of masonry structures, CISM international centre for mechanical sciences, Springer, 551, 1–26, doi: 10.1007/978–3–7091–1774–3.

ASTM (2001). Standard test method for determination of rock hardness by rebound hammer method. ASTM Stand. 04.09 (D 5873–00).

Avni R. (1999). The 1927 Jericho Earthquake. Comprehensive Macroseismic Analysis Based on Contemporary Sources. Ben Gurion University of the Negev, Beer Sheva (in Hebrew).

Azzam M., F. Doukh (2009). Site investigation for Saint Stylite Tower at Um er–Rasas/Madaba. Annex 1: Geological report for the Stylite Tower. Technical Report, Natural Resources Authority, Amman (Jordan).

Bender F. (1974). Geology of Jordan. Gebruedre, Berlin. 196 p.

Bongiovanni G., G. Buffarini, P. Clemente, D. Rinaldis and F. Saitta (2017). Experimental vibration analyses of a historic tower structure. J. Civil Structural Health Monitoring, Springer, 7(5), 601–613, doi: 10.1007/s13349–017–0245–4.

Bongiovanni G., G. Buffarini, P. Clemente and F. Saitta (2014). Ambient vibrational analysis of Aurelian Column. Proc. 10th U.S. National Conf. on Earth. Eng. (10NCEE, Anchorage, AK, 21–25 July), Paper 1013, EERI, doi: 10.4231.D35717P1T.

Bongiovanni G., Celebi M., Clemente P. (1990). The Flaminio Obelisk in Rome: vibrational characteristics as part of preservation efforts. Int. J. of Earth. Eng. and Structural Dynamics, 19(1), 107–118, John Wiley & Sons, doi: 10.1002/eqe.4290190110.

Buffarini G., P. Clemente, A. Paciello and D. Rinaldis (2008). Vibration Analysis of the Lateran Obelisk. Proc., 14th World Conf. on Earth. Eng. (14WCEE, Beijing, 12–17 Oct), Paper S11–055, IAEE & CAEE, Mira Digital

Publishing, Saint Louis.

Buffarini G., P. Clemente, A. Paciello and D. Rinaldis (2009). The Lateran Obelisk: Experimental analysis and modelling. In Mazzolani F.M. (ed), Protection of Historical Buildings, PROHITECH 09 (Proc. Int. Conf. on Protection of Historical Buildings, Rome, Italy, 21–24 June), 1, 841–848, Taylor & Francis Group, London.

Bongiovanni G., G. Buffarini P. Clemente, D. Rinaldis and F. Saitta (2017). Dynamic Characteristics of the Amphitheatrum Flavium northern wall from traffic–induced vibrations. Annals of Geophysics, 60(4), S0439, INGV, Rome, doi: 10.4401/ag–7178.

Byerlee J. (1978). Friction of rocks. Pure Appl. Geophys., Vol. 116, 4–5, 615–626, 1978.

Chopra A.K. and R.K. Goel (2002). A modal pushover analysis procedure for estimating seismic demands for buildings. Earthquake Engineering and Structural Dynamics, 31, 561–582, doi: 10.1002/eqe.144.

Clemente P., G. Bongiovanni and G. Buffarini (2002). Experimental analysis of the seismic behaviour of a cracked masonry structure. Proc., 12th European Conference on Earthquake Engineering (London, 9–13 Sept.), Paper No. 104, Elsevier Science Ltd.

Clemente P., F. Saitta, G. Buffarini and L. Platania (2015) Stability and seismic analyses of leaning towers: the case of the minaret in Jam. The Structural Design of Tall and Special Buildings, 24, 40–58, Wiley, doi: 10.1002/tal.1153.

Cozzolino M., R. Gabrielli, P. Galatà, V. Gentile and G. Greco (2019). Combined use of 3D metric surveys and non–invasive geophysical surveys for the determination of the state of conservation of the Stylite Tower at Umm ar–Rasas, Jordan. Annals of Geophysics, This issue; doi: 10.4401/ag–8060.

De Stefano A., E. Matta and P. Clemente (2016). Structural health monitoring of historical heritage in Italy: some relevant experiences. J. of Civil Structural Health Monitoring, 6(1), 83–106, Springer, doi: 10.1007/s13349–016–0154–y.

Desideri A., G. Russo, C. Viggiani (1997). The stability of towers on deformable ground. Rivista Italiana di Geotecnica, 1, 21–29.

Deere D.U. and R.P. Miller (1966). Engineering classification and index properties for intact rocks. Tech Rep Air Force Weapons Lab, New Mexico, no AFNL–TR, 65–116.

DOA, Department of Antiquities of the Hashemite Kingdom of Jordan (2002). The old city of Umm ar–Rasas (Mefa'a), Nomination file submitted to the World Heritage Bureau and Committee for inscription on the World Heritage List, Amman.

Dogangun A., R. Acar, H. Sezen, R. Livaoglu (2008). Investigation of dynamic response of masonry minaret structures, Bulletin of Earthquake Engineering, 6, 505–517.

Dweirj M., F. Fraige, H. Alnawafleh, A.Titi (2017) Geotechnical Characterization of Jordanian Limestone. Geomaterials, 7, 1–12.

EN 12504–2 (2012). Testing concrete in structures. Non–destructive testing. Determination of rebound number. European standardization, Brussels, Belgium.

Fajfar P. (2000). A Nonlinear Analysis Method for Performance Based Seismic Design. Earthquake Spectra, 16(3), 573–592.

Fener M., S. Kahraman, A. Bilgil, O. Gunaydin (2005). A comparative evaluation of indirect methods to estimate the compressive strength of rocks. Rock Mech. Rock Eng., 38(4), 329–343.

Gallipoli M., M. Mucciarelli, R. Castro, G. Monachesi, P. Contri (2004). Structure, soil–structure response and effects of damage based on observations of horizontal–to–vertical spectral ratios of microtremors. Soil Dynamics and Earthquake Engineering. 24. 487–495, doi: 10.1016/j.soildyn.2003.11.009.

Gentile C., and A. Saisi (2002). Ambient vibration testing of historic masonry towers for structural identification and damage assessment. Construction and Building Materials, 21(6), 1311–1321.

Gosar A., J. Rošer, B. Šket Motnikar, P. Zupan i (2010). Microtremor study of site effects and soil–structure resonance in the city of Ljubljana (central Slovenia). Bulletin of Earthquake Engineering, 8 571–592, doi: 10.1007/s10518–009–9113–x.

Haciefendioğlu K., F. Birinci (2011). Stochastic dynamic response of masonry minarets subjected to random blast and earthquake–induced ground motions. The Structural Design of Tall and Special Buildings, 20, 669–678.

ISRM (1978). Suggested methods for determining hardness and abrasiveness of rocks. Int. J. Rock Mech. Min. Sci. Geomech. Abstracts, 15, 89–98.

Ivorra S. and F.J. Pallarés (2006). Dynamic investigations on a masonry bell tower. Engineering Structures, 28(5), 660–667.

Katz O., Reches Z., Roegiers J.C. (2000). Evaluation of mechanical rock properties using a Schmidt Hammer. Int J Rock Mech Min Sci, 37, 723–72.

Konno K., T. Ohmachi (1998). Ground–motion characteristics estimated from spectral ratio between hori-

zontal and vertical components of microtremor. Bulletin of the Seismological Society of America, 88(1), 228–241.

Krstevska L., L. Tashkov, N. Naumovski, G. Florio, A. Formisano, A. Fornaro, R. Landolfo (2010). In–situ experimental testing of four historical buildings damaged during the 2009 L'Aquila earthquake. COST ACTION C26: Urban Habitat Constructions under Catastrophic Events – Proceedings of the Final Conference, 427–432.

Margottini C., D. Spizzichino, A. Sonnessa, L.M. Puzzilli (2015). Natural hazard affecting the Katskhi Pillar Monastery (Georgia). Eng. Geol. Soc. Territ., 8, 393–397.

Menahem A.B. (1991). Four Thousand Years of Seismicity Along the Dead Sea Rift. Journal of Geophysical Research, 96(B12), 20195–20216.

Miller R.P. (1965). Engineering classification and index properties for intact rock, PhD thesis, University of Illinois.

Modena C., M.R. Valluzzi, R. Tongini Folli, L. Binda (2002). Design choices and intervention techniques for repairing and strengthening of the Monza cathedral bell–tower. Construction and Building Materials, 16, 385–395.

Mortezaei A., A. Kheyroddin, H.R. Ronagh (2010). Finite element analysis and seismic rehabilitation of a 1000–year–old heritage listed tall masonry mosque. The Structural Design of Tall and Special Buildings, 21, 334–353.

Naghoj N.M., N.A.R. Youssef, O.N. Maaitah (2010). Mechanical Properties of Natural Building Stone: Jordanian Building Limestone as an Example, Jordan Journal of Earth and Environmental Sciences, 3(1), 37–48.

Nakamura Y. (1989). A method for dynamic characteristics estimation of subsurface using microtremor or the ground surface. Quarterly Report of RTRI 30 (1): 25–33.

Nakamura Y., E. D. Gurler, J. Saita (1999). Dynamic Characteristics of Leaning Tower of Pisa using microtremor–preliminary results. Proceedings of 25th JSCE Earthquake Engineering Symposium, 2, 921–924.

Oliveira C.S., E. Çakt , D. Stengel, M. Branco (2012). Minaret behavior under earthquake loading: The case of historical Istanbul. Earthquake Engineering and Structural Dynamics, 41, 19–39.

Peña F., P.B. Lourenço, N. Mendes, D.V. Oliveira (2010). Numerical models for the seismic assessment of an old masonry tower. Engineering Structures, 32, 1466–1478.

Picotti S., L. Sirovich, F. Pettenati, M. Giorgi, J. Carcione, M. Mucciarelli and A. Affatato (2012). Hints on the dynamic behaviour of the rocky tower of Montanaia Valley (Friulan Dolomites). XXXI Convegno Nazionale Gruppo Nazionale di Geofisica della Terra Solida GNGTS, Potenza, 20–22 November 2012

Powell J.H. (1989). Stratigraphy and sedimentation of the Phanerozoic rocks in central and south Jordan. Natural Resources Authority, Geological Mapping Division, Amman. 130 pp.

Sachpazis C.I. (1990). Correlating Schmidt hardness with compressive strength and Young's modulus of carbonate rocks. Bull. Int. Assoc. Eng. Geol., 42, 75–84.

Sadaqah R.M. (2000). Phosphogenesis, Geochemistry, Stable Isotopes and Depositional Sequences of the Upper Cretaceous Phosphorite Formation in Jordan. PhD thesis, University of Jordan, Amman. 257 pp.

Sarhosis V., G. Milani, A. Formisano, F. Fabbrocino (2018). Evaluation of different approaches for the estimation of the seismic vulnerability of masonry towers. Bulletin of Earthquake Engineering, 16 (3), pp. 1511–1545, doi: 10.1007/s10518–017–0258–8.

Sbeinati M.R., R. Darawcheh., M. Mouty (2005). The historical earthquakes of Syria: an analysis of large and moderate earthquakes from 1365 B.C. to 1900 A.D. Annals of Geophysics, 48(3), 347–435.

SESAME (2004). Guidelines for the implementation of the H/V spectral ratio technique on ambient vibrations–Measurements, processing and interpretation. SESAME European research project, Deliverable D23. 12., Project No. EVG1–CT–2000–00026 SESAME, 62 pp.

Tarawneh B. (1985). The Geology of A–Hisa (Al I'na). Map Sheet No. 3151–I. Natural Resources Authority, Amman, Jordan.

Thomas R., T.M. Niemi, S.T. Parker (2007). Structural Damage from Earthquakes in the Second–Ninth Centuries at the Archaeological Site of Aila in Aqaba, Jordan. Bulletin of the American Schools of Oriental.

Vasconcelos G., P.B. Lourenço (2009). In–Plane Experimental Behavior of Stone Masonry Walls under Cyclic Loading. Journal of Structural Engineering, ASCE, 135(10), 1269–1277.

Zohar M., S. Marco (2012). Re–estimating the epicenter of the 1927 Jericho earthquake using spatial distribution of intensity data. Journal of Applied Geophysics, Elsevier, 82, 19–29.

*CORRESPONDING AUTHOR: Paolo CLEMENTE,
ENEA C.R. Casaccia,
Via Anguillarese 301, 00123 Rome
email: paolo.clemente@enea.it